Circuit-tunable sub-wavelength THz resonators: hybridizing optical cavities and loop antennas

B. Paulillo,[1,3] J. M. Manceau,[1] A. Degiron,[1] N. Zerounian,[1]
G. Beaudoin,[2] I. Sagnes,[2] and R. Colombelli[1,*]

[1]*Institut d'Electronique Fondamentale, Univ. Paris Sud, CNRS UMR8622, 91405 Orsay, France*
[2]*Laboratoire de Photonique et Nanostructures, CNRS UPR20, 91460 Marcoussis, France*
[3]*bruno.paulillo@u-psud.fr*
[*]*raffaele.colombelli@u-psud.fr*

Abstract: We demonstrate subwavelength electromagnetic resonators operating in the THz spectral range, whose spectral properties and spatial/angular patterns can be engineered in a similar way to an electronic circuit. We discuss the device concept, and we experimentally study the tuning of the resonant frequency as a function of variable capacitances and inductances. We then elucidate the optical coupling properties. The radiation pattern, obtained by angle-resolved reflectance, reveals that the system mainly couples to the outside world *via* a magnetic dipolar interaction.

© 2014 Optical Society of America

OCIS codes: (230.5750) Resonators; (160.3918) Metamaterials; (050.6624) Subwavelength structures; (260.3910) Metal optics; (260.3090) Infrared, far.

References and links

1. H.-T. Chen, J. F. O'Hara, A. K. Azad, A. J. Taylor, R. D. Averitt, D. B. Shrekenhamer, and W. J. Padilla, "Experimental demonstration of frequency-agile terahertz metamaterials," Nat. Photon. **2**(5), 295–298 (2008).
2. B. Reinhard, O. Paul, R. Beigang, and M. Rahm, "Experimental and numerical studies of terahertz surface waves on a thin metamaterial film," Opt. Lett. **35**(9), 1320–1322 (2010).
3. G. Scalari, C. Maissen, D. Turcinková, D. Hagenmüller, S. De Liberato, C. Ciuti, C. Reichl, D. Schuh, W. Wegscheider, M. Beck, and J. Faist, "Ultrastrong coupling of the cyclotron transition of a 2D electron gas to a THz metamaterial," Science **335**(6074), 1323–1326 (2012).
4. D. Dietze, A. Benz, G. Strasser, K. Unterrainer, and J. Darmo, "Terahertz meta-atoms coupled to a quantum well intersubband transition," Opt. Express **19**(14), 13700–13706 (2011).
5. E. Strupiechonski, G. Xu, M. Brekenfeld, Y. Todorov, N. Isac, M. Andrews, P. Klang, C. Sirtori, G. Strasser, A. Degiron, and R. Colombelli, "Sub-diffraction-limit semiconductor resonators operating on the fundamental magnetic resonance," Appl. Phys. Lett. **100**(13), 131113 (2012).
6. E. Strupiechonski, G. Xu, P. Cavalié, N. Isac, S. Dhillon, J. Tignon, G. Beaudoin, I. Sagnes, A. Degiron, and R. Colombelli, "Hybrid electronic-photonic subwavelength cavities operating at terahertz frequencies," Phys. Rev. B **87**(4), 041408 (2013).
7. C. Walther, G. Scalari, M. I. Amanti, M. Beck, and J. Faist, "Microcavity laser oscillating in a circuit-based resonator," Science **327**(5972), 1495–1497 (2010).
8. A. A. Tavallaee, P. Hon, K. Mehta, T. Itoh, and B. S. Williams, "Zero-index terahertz quantum-cascade metamaterial lasers," IEEE J. Quantum Electron. **46**(7), 1091–1098 (2010).
9. K. Fan, A. C. Strikwerda, H. Tao, X. Zhang, and R. D. Averitt, "Stand-up magnetic metamaterials at terahertz frequencies," Opt. Express **19**(13), 12619–12627 (2011).
10. N. I. Zheludev and Y. S. Kivshar, "From metamaterials to metadevices," Nat. Mater. **11**(11), 917–924 (2012).
11. D. H. Staelin, A. W. Morgenthaler, and J. A. Kong, *Electromagnetic Waves* (Prentice Hall, 1994).
12. Y. Todorov, L. Tosetto, J. Teissier, A. M. Andrews, P. Klang, R. Colombelli, I. Sagnes, G. Strasser, and C. Sirtori, "Optical properties of metal-dielectric-metal microcavities in the THz frequency range," Opt. Express **18**(13), 13886–13907 (2010).
13. Y. Nga Chen, Y. Todorov, B. Askenazi, A. Vasanelli, G. Biasiol, R. Colombelli, and C. Sirtori, "Antenna-coupled microcavities for enhanced infrared photo-detection," Appl. Phys. Lett. **104**(3), 031113 (2014).
14. C. A. Balanis, *Antenna Theory: Analysis and Design* (Wiley, 2012).
15. D. Sievenpiper, R. F. J. Broas, N. G. Alexopolous, and E. Yablonovitch, "High-impedance electromagnetic surfaces with a forbidden frequency band," IEEE Trans. Microw. Theory Tech. **47**(11), 2059–2074 (1999).
16. Z. Chen, A. Megrant, J. Kelly, R. Barends, J. Bochmann, Y. Chen, B. Chiaro, A. Dunsworth, E. Jeffrey, J. Y. Mutus, P. J. J. O'Malley, C. Neill, P. Roushan, D. Sank, A. Vainsencher, J. Wenner, T. C. White, A. N. Cleland, and J. M. Martinis, "Fabrication and characterization of aluminum airbridges for superconducting microwave circuits," Appl. Phys. Lett. **104**(5), 052602 (2014).

17. S. Linden, C. Enkrich, M. Wegener, J. Zhou, T. Koschny, and C. M. Soukoulis, "Magnetic response of metamaterials at 100 terahertz," Science **306**(5700), 1351–1353 (2004).
18. N. Katsarakis, T. Koschny, M. Kafesaki, E. N. Economou, and C. M. Soukoulis, "Electric coupling to the magnetic resonance of split ring resonators," Appl. Phys. Lett. **84**(15), 2943 (2004).
19. K. Steinberg, M. Scheffler, and M. Dressel, "Microwave inductance of thin metal strips," J. Appl. Phys. **108**(9), 096102 (2010).
20. M. Husnik, M. W. Klein, N. Feth, M. König, J. Niegemann, K. Busch, S. Linden, and M. Wegener, "Absolute extinction cross-section of individual magnetic split-ring resonators," Nat. Photon. **2**(10), 614–617 (2008).
21. P. Lunnemann, I. Sersic, and A. Koenderink, "Optical properties of two-dimensional magnetoelectric point scattering lattices," Phys. Rev. B **88**(24), 245109 (2013).
22. W. Padilla, M. Aronsson, C. Highstrete, M. Lee, A. Taylor, and R. Averitt, "Electrically resonant terahertz metamaterials: Theoretical and experimental investigations," Phys. Rev. B **75**(4), 041102 (2007).
23. D. Schurig, J. J. Mock, and D. R. Smith, "Electric-field-coupled resonators for negative permittivity metamaterials," Appl. Phys. Lett. **88**(4), 041109 (2006).

1. Introduction

Reinterpreting and adopting well-established concepts from electronics and radio-frequency (RF) engineering in THz and mid-IR photonics is a challenge which can lead to innovations both in terms of conceptual advances and device concepts [1–6]. One distinctive outcome of this new trend is the emergence of structures that blur the line between photonics and electronics, offering unprecedented flexibility in terms of device compactness and frequency tunability [7–10]. Recently, hybrid electronic-photonic THz resonators with dimensions below the diffraction limit in all the three directions of space have been proposed by our team [5]. These devices permit deep sub-wavelength mode confinements as they support a fundamental resonance mediated by a real electrical current. The presence of a real electric current is crucial, since it allows one to decouple inductance and capacitance, which are in general intertwined in photonic cavities and also in standard transmission line resonators [11] (also called patch cavities [12] or patch antennas [13]). They are *de facto* topologically equivalents of split-ring resonators (SRRs) and they behave therefore as micrometric LC circuits while retaining key properties of standard photonic micro-cavities [6]. However, the extreme compactness of those resonators yields some drawbacks such as poor radiation coupling and a difficult inductive tuning, which might hinder their use for device applications.

In this paper, we address these limitations and further develop the aforementioned resonators. Thanks to an innovative fabrication technology (see pictorial representation in Fig. 1(a), the inductive section is now implemented as a metallic bridge suspended in air [Fig. 1(b)] and it is now endowed with the true functionalities of a loop antenna. The radiation frequency, coupling, polarization and efficiency are tailored *via* the sole design of the loop antenna, similarly to conventional RF designs. In turn, the capacitive section can host an "active" material, be it an emitter (a QC laser for instance), a detector (a quantum-well infrared detector, QWIP), or an absorber (a quantum well for polaritonic applications, for instance).

2. Device concept

The device concept is intuitively sketched in Fig. 1(a): a patch cavity of side s on a metallic ground plane is connected to a loop antenna [14]. Thanks to the presence of the metallic ground plane, and exploiting the mirror symmetry, this is equivalent to fabricating just half of the antenna. In an ideal picture, the patch cavity is a capacitive section (C) while the loop antenna is an inductive section (L), as shown in Fig. 1(a). This would yield a purely reactive impedance of the form $Z = i\omega L/(1-\omega^2 LC)$, given that the two components are connected in parallel [15].
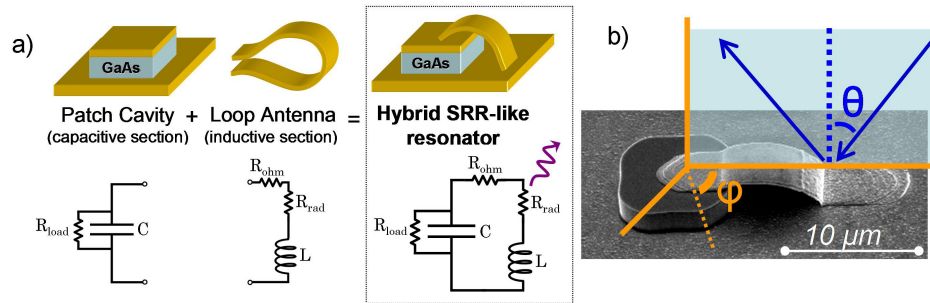
Fig. 1. (a) Intuitive idea of the hybrid loop-antenna/patch-cavity resonator. Equivalent circuit: the patch is mainly a capacitive section, while the antenna is mainly inductive. The antenna also features a radiative resistance (R_{rad}) which is responsible for radiation coupling. (b) Scanning electronic microscope (SEM) image of a real device. The superimposed schematic defines the incidence angles θ and φ.

To account for radiation coupling and losses, resistances must be introduced: R_{load} accounts for losses in the semiconductor region; R_{ohm} accounts for the losses induced by the loop and patch metal resistance; R_{rad} accounts for – importantly – the radiation coupling. As a matter of fact, this hybrid resonator can be seen as a loop antenna with complex impedance $Z_{ant} = R_{ohm} + R_{rad} + i\omega L$, connected to a capacitive load formed by the two metallic plates with complex impedance $Z_{load} = R_{load}/(1 + i\omega\,R_{load}C)$.

Contrary to [6], where the loop antenna was resting on a 1-µm-thick SiO_2 insulation layer on the device top and sidewalls, the loop is now defined as a suspended metallization (Fig. 1). To create the metal loops we adapted a fabrication procedure for air bridge structures, widely employed in microwave technology [16]. A scaffold for the bridge is formed using a positive photoresist (Shipley S1818) before defining lithographically the metal stripe (AZ5214 image reversal photoresist is used in this step). The height of the bridge is set by the resist thickness while the width, length and position of the bridge are set by photolithography.

This approach has important implications, as it permits a flexible and efficient control of the impedance parameters listed above.

The antenna inductance L is linked to the length of the suspended metallization, which we can now control independently of the capacitive section. The inductance sets the resonance frequency via the known formula $f = 1/2\pi(LC)^{1/2}$, hence it is possible to set the operating wavelength via the sole inductance, in complete independence from the semiconductor core size which can therefore be extremely sub-wavelength. R_{rad}, the radiation resistance of the antenna, is the key parameter which sets the radiation coupling properties of the system. For a loop antenna it is approximately proportional to the square of the surface enclosed by the loop [14], which can be almost freely set as shown in the right insets of Fig. 2. This is a major progress with respect to the devices in [6], which were typically under-coupled given the lack of freedom in the engineering of R_{rad}.

In order to explore and validate the aforementioned properties, we have fabricated a series of samples whose characteristics are summarized in Fig. 2. The material used is undoped GaAs, grown by MOCVD, whose thickness t is kept constant at 2 µm for this demonstration and it is sandwiched between two metallic plates (metal-insulator-metal, MIM, configuration). The loop antennas are made of Ti/Au and their widths and thicknesses are 4 µm and 250 nm, respectively. The device density is approximately 2400 dev/mm².

	6.5 µm	7.5 µm	8.5 µm	9.5 µm
9 µm	**1.65 THz** 182 µm	**1.39 THz** 215 µm	**1.18 THz** 253 µm	**1.03 THz** 290 µm
7 µm	**1.80 THz** 167 µm	**1.53 THz** 196 µm	**1.32 THz** 227 µm	**1.14 THz** 263 µm
5 µm	**2.10 THz** 143 µm	**1.75 THz** 171 µm	**1.47 THz** 204 µm	**1.29 THz** 233 µm
3 µm	**2.64 THz** 114 µm	**2.10 THz** 143 µm	**1.77 THz** 170 µm	**1.53 THz** 196 µm

Loop Length (l)
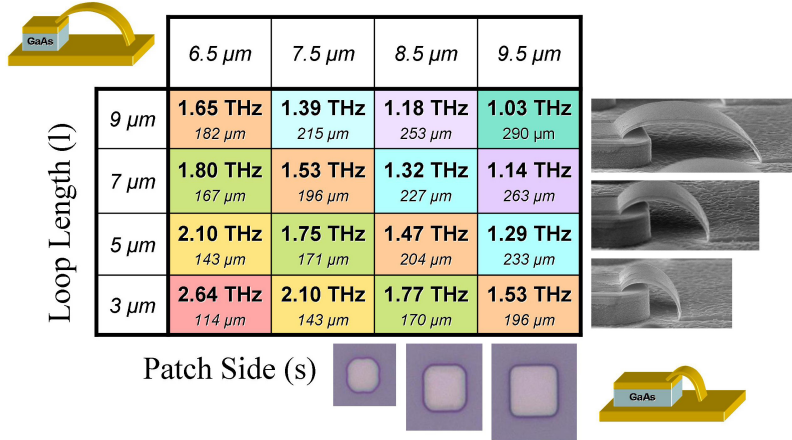
Patch Side (s)

Fig. 2. Specifications of the fabricated devices: 16 device geometries were fabricated (a 4x4 matrix) with 4 different patch side (*s*), and 4 different loop antenna lengths (*l*). The GaAs thickness *t* is kept constant at 2 µm. The operating frequency (wavelength) of the fundamental LC mode of each device is reported in the corresponding matrix cell. The colors identify the nominally *iso-frequency* samples. Details about how the cavities were measured are given in section 3.

The guiding idea was to independently vary the inductance (the loop length) or the capacitance (the patch dimension) in order to exhaustively study the properties of the system. In particular, we aimed at implementing sets of *isofrequency* devices, i.e. devices with nominally identical operating frequencies, but different structural parameters. In Fig. 2 – which summarizes the *experimental* operating wavelengths/frequencies of the fundamental LC resonance – these device sets are highlighted with identical colors. This shows that L and C can be controlled in total independence, and – for a given frequency – the device geometry can be optimized to suit a specific application. For instance, capacitance dominated devices will be useful for developing sub-wavelength lasers, since a large amount of gain is necessary, and the optical gain is located in the active semiconductor core. On the other hand, inductance dominated devices will be useful for detectors, since the extremely small surface of the active core can lead to reduced dark currents.

3. Device characterization: circuit tuning of the resonant frequency *via* L and C

The photonic eigenvalues of the system can be probed by polarized, angle-resolved reflectivity measurements, which were performed – under vacuum – with a Fourier transform infrared spectrometer (FTIR). A gold coated mirror of the same dimension of the samples has been used as reference to normalize the reflectivity spectra. Because the spot size S of the THz beam is much larger than individual structures, we fabricated and characterized periodic arrangements of identical cavities that were larger than *S* so as to maximize the signal/noise ratio. The period of the arrays is largely sub-wavelength to forbid all the diffractive orders except the 0th-order reflection.

Figure 3(a) summarizes the 4 independent experimental configurations (two sample orientations and two polarizations) which were explored for the characterization of the devices. Figure 3(b) reports the reflectivity measurements on a typical device, for the four measurement conditions highlighted (θ = 45°). The resonant modes appear as sharp resonances in the reflectance spectra.
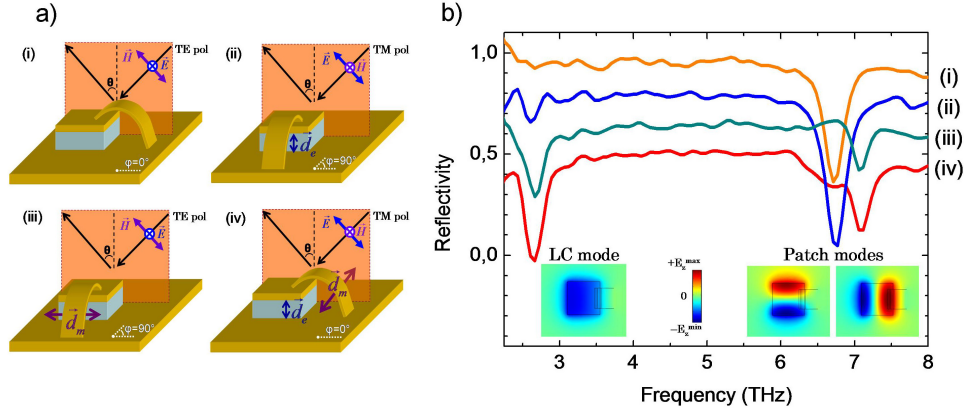
Fig. 3. (a) Experimental configurations for device characterization. The arrangement of the E,H fields with respect to the incidence plane is highlighted for TM, TE polarizations. The twist angle φ identifies the two non-equivalent orientations of the loop antenna: φ = 0° parallel to the incidence plane, φ = 90° normal to the incidence plane. (b) Typical reflectivity spectrum at 45° for a device in the 4 configurations. Spectra are stacked (offset ≈-0.2) for the sake of clarity. The top spectrum is not shifted and it shows that the background reflectivity is close to unity. The dip around f≈7 THz is the patch TM_{001}/TM_{010} mode. For configurations (ii) - (iv) the LC mode appears at ≈2.6 THz. The E_z field distribution at resonance in the semiconductor is shown in the insets.

The two modes at ≈7 THz are the dominant TM_{001}/TM_{010} modes of a standard MIM patch cavity, whose electric field z-component distribution is represented in the right inset of Fig. 3(b). Their wavelength is related to the patch side as $\lambda_{eff} = \lambda/n_{eff} = 2 \cdot s$, i.e. the situation when one half internal wavelength corresponds to the cavity side. n_{eff} is an effective index which takes into account the dielectric constant of the material sandwiched by the metallic plates, *and* the phase of the reflectivity at the cavity edges [12]. However, when the semiconductor material is etched around the cavity, the reflectivity phase effect is marginal. The degeneracy of the two fundamental patch modes is split by the presence of the metallic bridge [5].

The low-frequency mode at f≈2.6 THz is instead the fundamental LC mode of the structure, characterized by a (quasi) uniform AC electric field between the two metal plates, as clearly shown in the left inset of Fig. 3(b). This mode exhibits the well-known coupling selection rules of split ring resonators [17,18], as shown in Fig. 3(b). In configuration (ii) the incoming wave excites the LC resonance by inducing an AC voltage (or charge separation) over the capacitive section via the electric field normal to the metal plates (induced vertical electric dipole, d_E). In configuration (iii) a circulating AC current is instead excited in the loop antenna by the magnetic field normal to the loop plane (induced horizontal magnetic dipole moment, d_M). Both d_E and d_M are excited in configuration (iv) yielding a stronger coupling to the LC mode. No coupling to the LC mode is observed in configuration (i).

Figure 4 reports the frequency of the LC modes for all the fabricated resonators, as a function of the patch side *s* and of the antenna length *l*.

The operating wavelength of the devices increases linearly with the patch side *s*. This in agreement with the formula $f = c/\lambda = 1/2\pi(LC)^{1/2}$, since the square root of *C* is proportional to *s*. For a fixed patch side, the operating frequency increases with the inductor length. This is again in agreement with the aforementioned formula. Note that in all cases, the resonance frequency of the LC mode is much lower than what is allowed by the diffraction-limited patch cavity alone, $s = \lambda_{eff}/2$. This leads to extremely low effective electromagnetic volumes, also due to the very thin semiconductor core employed. For instance, the resonator with s = 9.5 μm and l = 9 μm, we have $V_{eff} = 2 \times 10^{-3} (\lambda/2 \cdot n_{eff})^3$.
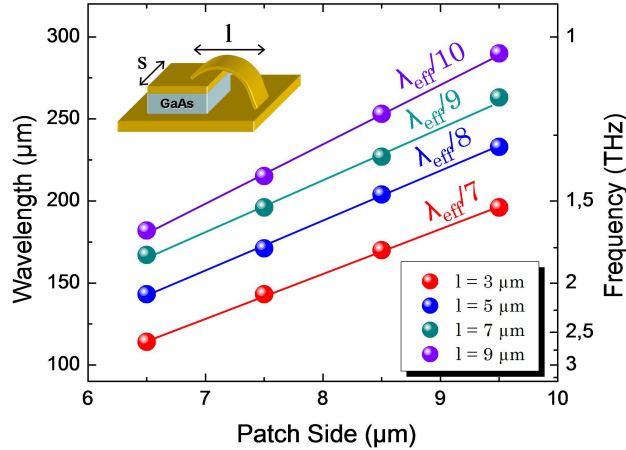
Fig. 4. Experimental wavelengths (frequencies) of the LC mode as a function of the patch side (*s*) for various inductor lengths (*l*). For a fixed loop size the trend is linear, as expected from theory. The confinement ratio in the semiconductor, λ_{eff}/s, is reported for each inductor size. A value of 2 corresponds to the diffraction limit.

As a matter of fact, the simple LC model is remarkably quantitative. The capacitance C_s of a MIM patch of *area S* and GaAs thickness $t = 2\ \mu m$ can be estimated as $C_s = \varepsilon_0\ \varepsilon_{GaAs}\ S/t$. Similarly, the inductance L_l of the antenna loop of length l can be estimated based on the analytical model in [19] considering the width, thickness and total length of the metallic stripe. All the resulting values are reported in Fig. 5, top panel, and a comparison between the experimental (full dots) and the analytically calculated (open stars) operating wavelengths is reported in the body of Fig. 5.
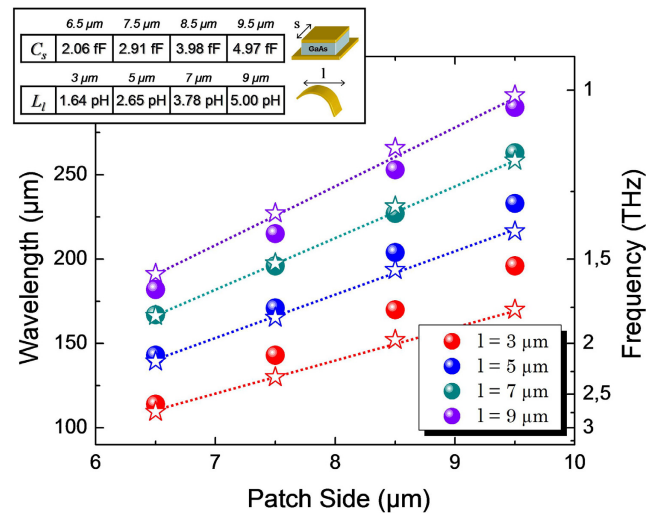
Fig. 5. Resonant wavelengths (frequencies) of the LC mode obtained with a simple, parameter-free LC model (open stars) compared to the experimental data from the reflectivity measurements (full dots). The inset reports the values of the patch capacitance C_s *(fF)* and of the loop inductance L_l *(pH)* as obtained from the sample geometrical parameters.

The agreement is very good, considering that no adjustment parameter is employed. For short values of the inductance length *l* a discrepancy occurs though, possibly because the loop length becomes comparable to its width. Moreover, it is more difficult to clearly separate the system into a capacitive section and an inductive one. In any case, the predictive character of

a very simple LC model is a major improvement with respect to our previous realizations in [5,6]. It also stems from the almost complete spatial separation between the electric-field and magnetic-field regions of the device which truly behaves like a lumped-element resonator. On one hand, we can now set the operating frequency of the system at will, by choosing the correct antenna loop dimension. On the other hand, a simple, but reliable LC model is a precious tool for device design.

4. Optical coupling: radiation patterns, magnetic dipole coupling, Q-factors

In order to characterize the spatial absorption properties and the quality factors of the hybrid resonators, reflectivity spectra for incidence angles ranging from 15° to 60° were collected for various samples. The width and depth of the reflectance dips were then estimated from Lorentz fits of the spectra around the LC resonance. The peak absorbed intensity is calculated as $A = 1-R_{min}$, with R_{min} the minimum reflectivity value (reached at resonance).

We first discuss the magnetic dipole interaction. Figure 6(a) reports typical angle-resolved spectra for a sample having $s = 7.5\ \mu m$ and $l = 5\ \mu m$ and for the experimental configuration (iii), as shown in the inset.
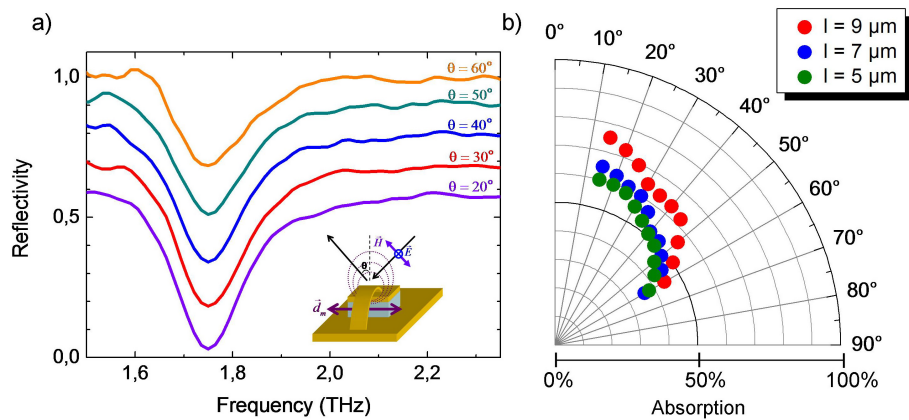
Fig. 6. (a) Typical reflectivity spectra at different incidence angles (sample $s = 7.5\ \mu m$, $l = 5\ \mu m$) in the experimental configuration shown in the inset (iii). Spectra are stacked (offset ≈-0.1) for the sake of clarity. The top spectrum is not shifted and it shows that the background reflectivity is close to unity. (b) Polar plot of the absorbed intensity vs incidence angle for three devices having constant patch size ($s = 7.5\ \mu m$) and different loop lengths.

The absorption is maximal for quasi-normal incidence and reduces at grazing angles. This behaviour is easily understood remembering that the antenna acts like an elementary inductive loop which couples to the magnetic field normal to its plane.

To strengthen the conclusion, Fig. 6(b) plots in a polar diagram the peak absorbed intensity A as a function of the incidence angle θ for three samples having constant patch side ($s = 7.5\ \mu m$), but different loop lengths l. The absorption angular pattern is clearly reminiscent of the power pattern of a small loop antenna having a null normal to the plane of the loop and a maximum along its plane [14]. The maximum measured peak absorption is ~70% at (quasi) normal incidence.

For a more quantitative analysis of the magnetic dipole coupling, similar polar diagrams are reported in Fig. 7 for the three quasi-isofrequency LC resonators operating around 1.8 THz (see Fig. 2 - green diagonal). Figure 7(b) highlights that, at fixed operating frequency, a larger loop permits a stronger radiation coupling. A simple explanation is that the magnetic dipole moment associated to an elementary current loop is proportional to the surface enclosed by the loop itself. In RF engineering this is accounted for by the antenna radiation resistance R_{rad} which – for a small loop – is $\sim S^2/\lambda^4$ (S is the surface enclosed by the loop and λ the operating wavelength).

To demonstrate that the measured absorption pattern indeed originates from the small loop antenna (or – equivalently – its magnetic dipole d_M), we plot in Fig. 7(c) the absorption pattern $A(\theta)$ normalized to the extrapolated maximum absorption at 0°. All the three data sets superpose and they are well fitted by a $cos(\theta)$ function. A $cos^2(\theta)$ angular dependence is expected according to the well-known normalized power pattern of a small magnetic dipole. In fact, to obtain the actual absorption strength of a sub-wavelength scatterer we must compute the ratio σ/S, σ being the cross section of the object and S the area of the impinging focused (Gaussian) beam [20]. The actual scattering properties of a single LC resonator are therefore described by an effective extinction cross section of the form $\sigma_{ext}(\theta) \propto A(\theta)\, cos(\theta)$ [21], where $cos(\theta)$ accounts for the broadening of the excitation beam with the incidence angle. The measured absorption data $A(\theta) \propto cos(\theta)$ therefore correctly lead to a cross section $\sigma_{ext}(\theta)$ with the expected dipolar dependence $cos^2(\theta)$.
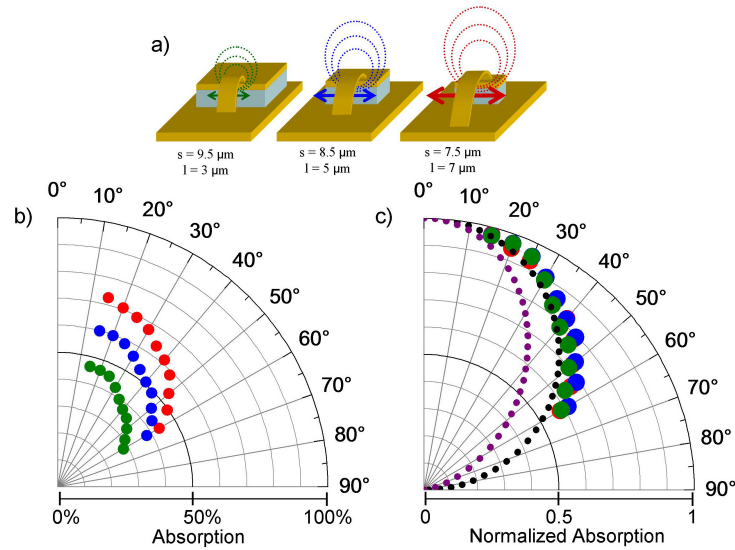
Fig. 7. (a) Schematics and dimensions of the *iso-frequency* resonators analyzed. (b) Polar plot of the absorption *vs* incidence angle. (c) Normalized absorption patterns. For comparison, a $cos(\theta)$ fit (black dotted line) and a $cos^2(\theta)$ fit (purple dotted line) are shown. The data clearly follow a $cos(\theta)$ dependence.

We now discuss the excitation of the LC resonance through electric dipole coupling. Figure 8(a) reports the angle-resolved spectra for a sample having $s = 6.5\ \mu m$ and $l = 3\ \mu m$ and for the experimental configuration (ii). The absorption is minimal for quasi-normal incidence and grows at grazing angles (note: the angular range is here extended up to 80°). This happens because the electric field component parallel to the patch sidewalls increases with the incidence angle. This field component excites a charge oscillation at the metal plates of the patch which in turn behaves like an elementary electric dipole.

The polar diagram in Fig. 8(b) reports the angular dependence of the absorption which is of the form $sin^2(\theta)/cos(\theta)$, where the factor $1/cos(\theta)$ is introduced following the argument discussed in the previous paragraph. The resulting cross section $\sigma_{ext}(\theta)$ yields the power dependence $sin^2(\theta)$, as expected for a sub-wavelength electric dipole. A similar trend is observed in the experimental configuration (iv) (data not shown) where an angle-dependent electric coupling adds to a constant magnetic coupling due to the TM incident field. An absorption larger than 90% has been measured in the latter configuration thanks to the sum of the electric and magnetic interactions.
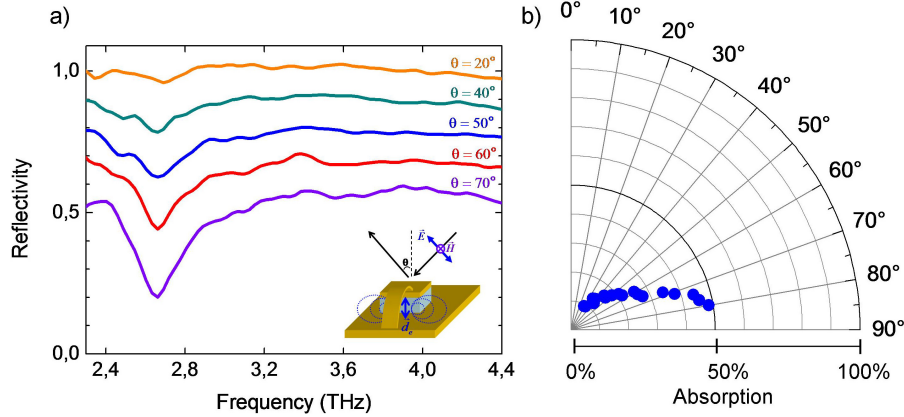
Fig. 8. (a) Reflectivity spectra at different incidence angles (sample $s = 6.5\ \mu m$, $l = 3\ \mu m$) in the experimental configuration shown in the inset (ii). Spectra are stacked (offset $\approx$-0.1) for the sake of clarity. The top spectrum is not shifted and it shows that the background reflectivity is close to unity. (b) Polar plot of the absorbed intensity vs incidence angle

The total quality factors (Q_{tot}) of the resonators can be extracted from the reflectivity measurements as $\omega_0/\delta\omega$, where ω_0 is the peak absorption frequency, and $\delta\omega$ is the FWHM. Q_{tot} is defined as $(1/Q_{rad} + 1/Q_{loss})^{-1}$, where Q_{rad} is the radiative Q (connected to R_{rad}) and Q_{loss} takes into account all the sources of loss (in the patch and in the antenna). The measured Q_{tot} for the 3 iso-frequency samples discussed in Fig. 7 are reported in Fig. 9, as a function of the measurement angle. Note: the measured Qs should be angle invariant. The observed decrease with increasing angle is possibly due to inhomogeneous broadening since the number of explored devices increases due to the $1/cos(\theta)$ factor.
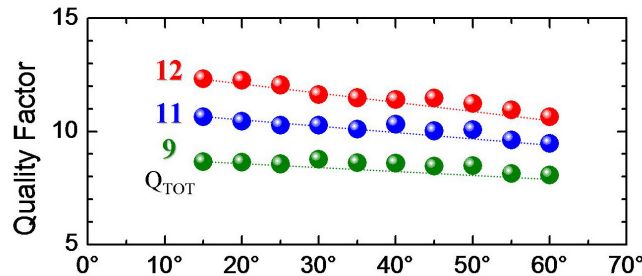
Fig. 9. Experimental Q-factors of the LC resonance for the three iso-frequency samples of Fig. 7 (red dots: $l = 7\ \mu m$; blue dots: $l = 5\ \mu m$; green dots: $l = 3\ \mu m$), as a function of the angle of incidence of the reflectivity measurement used to extract resonance width. In theory, the Q-factor should not change with the angle, since only the 0-order reflection is involved. The decrease at large angles is probably due to inhomogeneous broadening since the number of explored devices increases.

We observe that the Q-factor of the inductance dominated device is higher ($Q = 12$) than the one of the capacitance dominated device ($Q = 9$). However, it will be necessary to measure several more resonators operating at the same frequency to understand if this is indeed a peculiarity of this device architecture, or just a statistical fluctuation.

5. Playing with circuit concepts: inductances in parallel

In this section we further develop the circuital paradigm introduced so far to design hybrid THz resonators having user-tailored properties. Taking inspiration from the design of the electrically resonant split-ring resonators (eSRRs) [22, 23] we developed three classes of devices as shown in Fig. 10. For their realization 1.5 μm thick undoped GaAs was used as dielectric core for the circular patch. Here the diameter of the capacitive section is kept

constant at 7 μm as well as the width and thickness of the metallic loops (3.5 μm and 0.25 μm respectively). The only geometric parameter used to tune the operating LC frequency is the length l of the loops ranging from 3 μm to 6.5 μm.
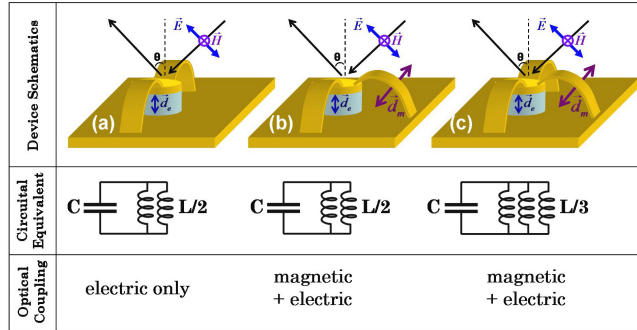
Fig. 10. Schematics of 2 and 3 inductor devices based on eSRR concept. The experimental configuration (incidence plane, polarization) used for characterization is also sketched. Equivalent circuits and allowed optical coupling are specified.

Resonator (a) implements in 3D the basic 2D eSRR [18], with two inductive loops connected to the capacitive section at 180° angle. From a circuital point of view, the addition of a second inductor L yields a resonance blueshift to the value $f = \sqrt{2}/2\pi(LC)^{1/2}$, being $L/2$ the equivalent inductance of two identical inductors connected in parallel. However, due to the symmetry of this design, radiation can excite the LC mode only *via* electric dipolar coupling, as the two antenna magnetic dipoles cancel each other. The measured spectra (data not shown) show in fact – similarly to Fig. 8 – weak absorption except at grazing incidence angles. These devices have obviously a very high Q_{rad}, but the measured Q_{total} is similar to one-inductance ones. This finding confirms that these resonators are still electromagnetically undercoupled.

In design (b) two inductors are instead connected to the patch cavity at 90° angle. While the resonant frequency is of course the same as in (a), the magnetic coupling is restored because of symmetry breaking. Finally in (c) a third inductor is added in parallel ($L_{eff} = L/3$) allowing a further frequency blueshift to the value $f = \sqrt{3}/2\pi(LC)^{1/2}$.

The experimental reflectivity spectra of type (b) and (c) resonators for various inductor lengths, but *equal dimensions of the capacitive section*, are shown in Fig. 11(a). The data are normalized to highlight the wide frequency tuning of the LC resonance with the inductance loop length. The experimental resonant frequencies are plotted as a function of the inductor length l, and the mean ratio between the LC frequencies for a 3-loop and a 2-loop device of same l is $1.28 \approx \sqrt{3}/\sqrt{2}$, in excellent agreement with the circuital law for inductors in parallel.

The important conclusions here are that (i) a circuital approach allows one to span an extremely wide range of operating wavelengths (70 μm < λ < 215 μm in this case) without changing the semiconductor region volume, which is in this case fixed at a lateral size of 7 μm. In a hypothetical cavity electrodynamics experiment, this means keeping constant the number of active dipoles involved in the process. Or, in the case of a detector, keeping its active volume unvaried to a sub wavelength dimension irrespectively of the operating wavelength. And (ii) that we can engineer the radiation properties of these hybrid resonators (in terms of coupling and polarization) without modifying the semiconductor core.
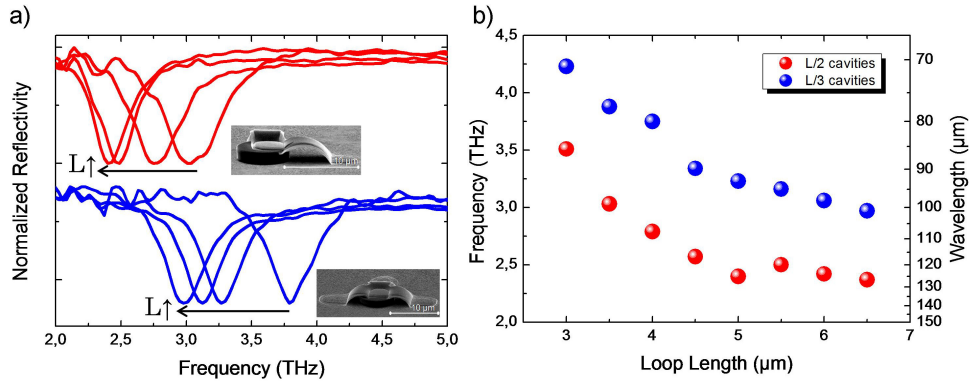
Fig. 11. (a) Reflectivity spectra (normalized) for 2 and 3 loop devices. Tuning of the LC resonance with inductance is shown. (b) LC frequencies (wavelengths) vs loop length for devices (b) $L_{eff} = L/2$ and (c) $L_{eff} = L/3$

7. Conclusions

We have demonstrated sub-wavelength electromagnetic resonators operating in the THz spectral range, whose spectral properties and spatial/angular patterns can be engineered in a similar way to an electronic circuit. The inductive section of the resonator is now implemented as a metallic bridge suspended in air (a loop antenna): as a consequence, the radiation frequency, coupling, polarization and efficiency are tailored *via* the sole design of the loop antenna, similarly to conventional RF designs.

Due to the versatility of our fabrication scheme, the proposed resonators are suitable for the realization of semiconductor/metal passive absorbers having user-designed electromagnetic response and they provide a flexible playground for cavity electrodynamics and intersubband polaritonics.

The next challenge is to enable them with electrical injection. This is essentially a technological problem, which involves a few additional processing steps to insulate the DC current-carrying section (the contact) from the RF-current-section (the antenna), *via* a THz transparent insulator like SiO_2 or BCB.

The possibility of current injection would enable integration with quantum-cascade lasers (QCLs) or quantum-well infrared photo-detectors (QWIPs) for ultrasmall sources and detectors. For instance, capacitance dominated devices (see lower-right outset in Fig. 1) will be useful for developing sub-wavelength lasers, since a large amount of gain is necessary, and the optical gain is located in the active semiconductor core. On the other hand, inductance dominated devices (see upper-left outset of Fig. 1) will be useful for detectors, since the extremely small surface of the active core can lead to reduced dark currents.

Acknowledgments